Magnetic Navigation System Utilizing Resonant Effect to Enhance Magnetic Field Applied to Magnetic Robots

Jaekwang Nam, Wonseo Lee, *Student Member, IEEE*, Bongjun Jang, and Gunhee Jang, *Member, IEEE*

***Abstract*—We propose a novel magnetic navigation system (MNS) with the resonant effect of an *RLC* circuit to generate large magnetic field in high frequency. The variable capacitors of the proposed MNS make it possible not only to change the resonant frequency of the *RLC* circuit, but also to maximize the output current without phase delay at variable resonant frequencies. The proposed MNS can compensate for the amplitude decrease and phase delay due to the inductance effect of a conventional MNS, while generating a uniform magnetic field with a wide range of rotating frequencies to effectively operate a helical robot in human blood vessels. For verification of the constructed MNS, we measured currents and magnetic fields at several resonant frequencies, and the experimental values corresponded well with the calculated values. We finally demonstrated that the proposed MNS substantially improves both moving and unclogging capabilities of a helical robot as compared to the conventional MNS.**

***Index Terms*—Magnetic navigation system (MNS), magnetic robot, resonant frequency, *RLC* circuit, rotating magnetic field.**

I. Introduction

MEDICAL robots capable of diagnosis and treatment in human organs have attracted a great deal of attention as an alternative to conventional surgical techniques. These robots require small entry routes to gain access to human organs like industrial robots working in pipes [1], [2], and their tasks in complex tissue environments necessitate a small-scale compact structure. Because medical robots are minimally invasive, many groups have studied the potential of medical robot use in various human organs. Electric robots utilizing various actuators and powered by electric cables have recently been examined [3]–[6]. Kim *et al.* developed a locomotive mechanism of capsule-type endoscopic robots using a shape-memory alloy to diagnose various diseases in the gastrointestinal tract [3]. Guo *et al.* proposed a fish-like robot utilizing an ionic conducting polymer film actuator [4]. Swimming smoothly in various aqueous environment, the robot can be used to perform diagnosis and surgery in the human body. Guozheng *et al.* studied a multijoint robot driven by a piezoactuator that can be equipped to perform diagnosis and treatment in human organs [5]. Dario *et al.* proposed a robot using a wobble-type electromagnetic microactuator for diagnosis of conditions in the colon [6]. While electric robots employing electric cables can be easily powered, the cables reduce steering capability in narrow and complex human organs, as the long rigid cables often impede steering of the robots. Although electric robots with wireless power systems have been considered as an alternative [7], [8], they require complex robot circuitry, which poses challenges for miniaturization. In addition, electric robots present the risk of electric shock in humans. To overcome these issues, magnetic robots wirelessly manipulated via magnetic fields of magnetic navigation systems (MNS) have been suggested for various medical applications [9]–[11]. Kim and Ishiyama studied spiral-type magnetic robots, which contain drugs loaded between dual spiral bodies, for targeted drug delivery in digestive organs [10]. Yim *et al.* developed a soft-capsule type magnetic robot that can release drugs at specific locations in the gastrointestinal tract [11].

Many researchers have attempted to utilize magnetic robots for treatment of coronary artery disease, as it is one of the major causes of human death in modern society [12]. One of the conventional treatments for coronary artery disease is a surgical intervention that employs a physician-controlled catheter to unclog blocked blood vessels. Typically, these catheters are difficult to steer due to long rigid guide wires. Wirelessly-manipulated magnetic robots, however, can effectively self-steer through narrow tortuous human blood vessels. Various bioinspired robots [13], [14] have been proposed. In particular, helical robots, inspired by Escherichia coli bacteria, present one of the most intriguing classes of robots. Because of their simple structure and sufficient controllability using a rotating magnetic field, helical robots have a great potential for unblocking obstructed blood vessels. There are three types of helical robots, sorted by blade shape: helix, screw, and twist [15]. For human blood vessels, magnetic robots with screw and twist blades are generally proposed, as they have large inner spaces that often contain magnets to increase the magnetic torque. Conversely,

Manuscript received January 24, 2016; revised September 28, 2016 and November 15, 2016; accepted December 31, 2016. Date of publication February 15, 2017; date of current version May 10, 2017. This work was supported by the National Research Foundation of Korea grant funded by the Korean Government (MSIP) (No. 2015R1A2A1A05001837). *(Corresponding author: Gunhee Jang.)*

The authors are with the Department of Mechanical Convergence Engineering, Hanyang University, Seoul 04763, South Korea (e-mail: njk0651@naver.com; justinleews@gmail.com; stern89@naver.com; ghjang@hanyang.ac.kr).

Color versions of one or more of the figures in this paper are available online at http://ieeexplore.ieee.org.

Digital Object Identifier 10.1109/TIE.2017.2669886

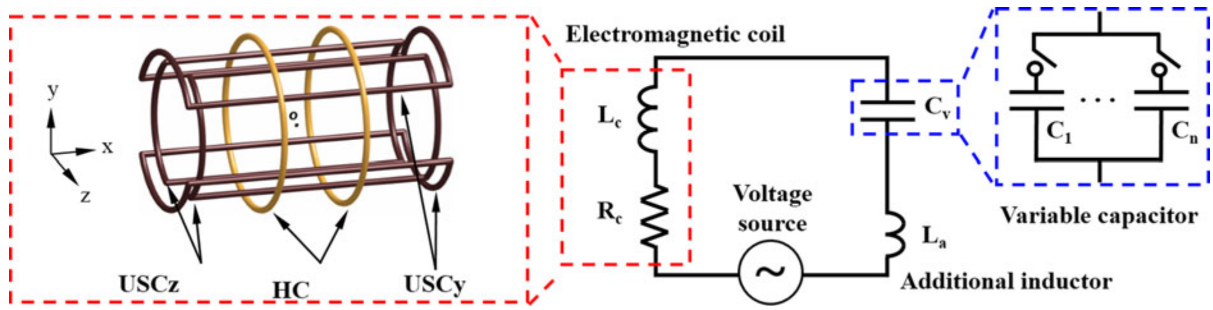

Fig. 1. Proposed MNS with three orthogonal pairs of coils with *RLC* circuits (the additional inductor is only included in HC).

helix blade-type robots typically employ a small magnetic head for actuation. Although helical robots with screw and twist blades generate greater magnetic torques than helix blade-type robots, the elevated magnetic torque values are still not sufficient to unclog most blood vessels. Therefore, many researchers have modified the basic helical robot to improve its unclogging ability [16]–[18]. Jeon *et al.* developed the double helical robot for drug delivery. This robot has drug-enhanced unclogging abilities utilizing the specific frequency range of the rotational magnetic field at the target point [16]. Jeong *et al.* proposed a helical robot utilizing a magnetic field gradient as well as a precessional magnetic field to increase propulsion force [17]. Kim *et al.* combined two helical robots to create a magnetic suspension structure between two helical robots such that the combined robot generates both propulsive force and additional pushing force using helical blades and a magnetic suspension structure [18]. Although these improved helical robots demonstrate enhanced drilling motion, MNS improvements are also effective for increasing drilling capability, as the magnetic torque is proportional to the external magnetic field generated by the MNS. Many researchers have developed various MNS and manipulation methods to control robots [19]–[22]. Kummer *et al.* developed an OctoMag, which has isotropic force control capabilities in every direction over the workspace using tracked position and robot orientation information [19]. Although the OctoMag is a well-designed system, it may not be appropriate for use with helical robots, as the design process did not include optimization of magnetic torque. Choi *et al.* suggested a MNS with three pairs of stationary Helmholtz coils (HC), a pair of stationary Maxwell coils, and a new mechanism for three-dimensional (3-D) drilling motion [20]. However, their geometric structure was not appropriate for use in the human body. Jeon *et al.* proposed a compact MNS that contains two saddle-shaped coil pairs to generate a uniform magnetic field and magnetic field gradient that is also suitable for use in humans [21]. Their MNS can generate isotropic magnetic torque over the workspace regardless of robot orientation or position. The group also investigated magnetic field generation by considering the inductance effect of the MNS that attenuates the amplitude and delays the phase of the current in proportion to the frequency of the applied voltage [22]. However, their system requires additional power and phase control to compensate for amplitude decreases and current phase delays.

In this paper, we proposed a novel MNS with the resonant effect of an *RLC* circuit to generate large magnetic field in variable high frequency without additional power and phase control. First, we mathematically investigated the magnetic field due to the inductance effect of the conventional MNS with three orthogonal coils [15]: a HC, and *y*- and *z*-directional uniform saddle coils (USC*y* and USC*z*). Next, we designed a novel MNS utilizing the resonant effect of an *RLC* circuit to generate a rotating magnetic field at a wide range of resonant frequencies, as shown in Fig. 1. Additionally, we built the proposed MNS and compared the actual magnitude and phase delay of the current and magnetic field with the calculated values. Finally, we performed several helical robot navigation and clogging experiments in tubular environments to verify the effectiveness of the proposed MNS.

II. MNS Utilizing the Resonant Effect of an RLC Circuit

A. Rotating Magnetic Field for a Helical Robot

A helical robot is manipulated by a magnetic torque generated by the product of the external magnetic field ($\mathbf{B_e}$) and the magnetic moment of a robot as follows [21]:

$$\mathbf{T}_e = \mathbf{m} \times \mathbf{B_e} \tag{1}$$

$$\mathbf{B_e} = \begin{bmatrix} (4/5)^{3/2} N_h i_h / r_h \\ 0.6004 N_{uy} i_{uy} / r_{uy} \\ 0.6004 N_{uz} i_{uz} / r_{uz} \end{bmatrix} \tag{2}$$

where μ_0, $\mathbf{m}$, N_k, i_k, and r_k are the magnetic permeability of free space, the magnetic moment of a robot, and the number of turns, current, and radius of the *k*th coil. The subscripts *h*, *uy*, and *uz* represent the HC, and *y*- and *z*-directional USCs, respectively. Fig. 2 shows the external rotating magnetic field able to propel a helical robot in the **N** direction. **N** is a unit vector along axial direction of the external rotating magnetic field. The magnetization direction of the permanent magnet inside the robot lies in the plane of the externally rotating magnetic field. This externally rotating magnetic field can be expressed as follows [23]:

$$\mathbf{B_e} = B_0 \left(\cos\omega t \mathbf{U} + \sin\omega t \mathbf{N} \times \mathbf{U}\right) \tag{3}$$

where B_0, ω, and $\mathbf{U}$ are the magnitude and angular velocity of the externally rotating magnetic field, and a unit vector from the origin toward a point on the circle, respectively. Utilizing the externally rotating magnetic field, a helical robot can generate

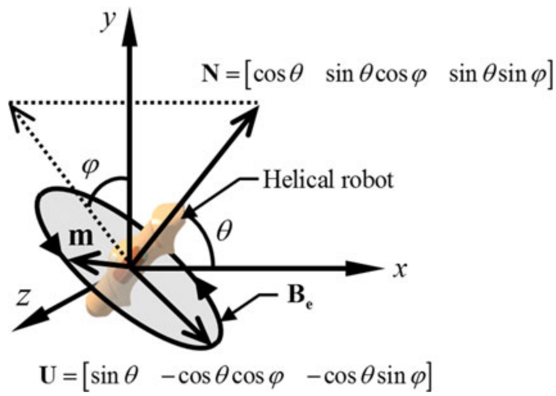

Fig. 2. External rotating magnetic flux density to propel a helical robot.

TABLE I
MAJOR VALUES OF THE MNS

	HC	USC*y*	USC*z*
Turns of the coil (turns)	430	320	400
Radius of the coil (mm)	216.0	133.8	167.5
Resistance of the coil (Ω)	23.7	15.1	32.2
Inductance of the coil (mH)	344.5	201.3	394.3
Maximum input voltage (V)	218.5	178.1	251.2
Maximum magnetic flux density (mT)	14.18	21.69	14.04

3-D helical motion that enables a helical robot to move to a target point and unblock the obstructed area.

B. Inductance Effect of the MNS

After applying the voltage to each coil of the MNS to generate a rotating magnetic field in (3), the input voltage and output current can be expressed as follows:

$$V = V_i \sin(2\pi f t) \tag{4}$$

$$I = I_o \sin(2\pi f t - \phi) \tag{5}$$

where V_i, f, I_o, and ϕ are the amplitude and frequency of the input voltage, and the amplitude and delayed phase of the output current, respectively. Using (4), (5) and the voltage equation of an *RL* circuit, the amplitude and delayed phase of the output current in the conventional MNS can be expressed as follows [24]:

$$I_o = \frac{V_i}{\sqrt{{R_c}^2 + (2\pi f L_c)^2}} \tag{6}$$

$$\phi = \tan^{-1}\left(\frac{2\pi f L_c}{R_c}\right) \tag{7}$$

where R_c and L_c are the resistance and inductance of a coil, respectively. Table I shows the major values of the conventional MNS. Using (2), (6), (7), and Table I, the amplitudes and phase delays of the magnetic field of the conventional MNS can be calculated as shown in Fig. 3. Fig. 3(a) shows the calculated amplitude of the magnetic field in which the amplitude decreases with an increase in an input voltage frequency due to the coil inductance effect, as shown in (6). Fig. 3(b) shows the calculated phase delay of the magnetic field in which the phase delay increases with an increase in the input voltage frequency due to the inductance effect, as shown in (7). In the conventional MNS, the rotating magnetic field has an elliptical trajectory because the amplitude and phase of the magnetic field generated by each coil have different values. Fig. 3(c) shows the rotating magnetic

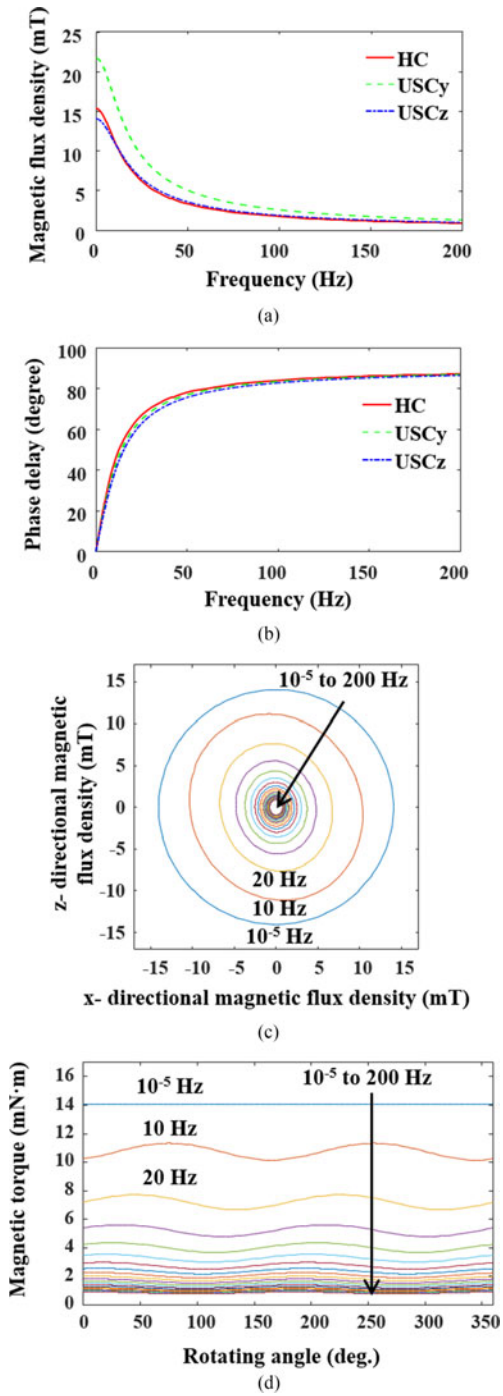

Fig. 3. (a) Magnetic flux density of each coil of the conventional MNS. (b) Phase delay of each coil of the conventional MNS. (c) Rotating magnetic field in the *xz*-plane, where the frequency varied from 10^{-5} to 200 Hz in increments of 10 Hz. (d) Magnetic torque ripple in the *xz*-plane applied to the helical robot, with a magnetic moment of 1 A · m^2.

field in the *xz*-plane, in which the rotating frequency increases from 10^{-5} to 200 Hz in increments of 10 Hz. At rotating frequencies close to 0 Hz, the rotating magnetic field has a circular trajectory with radius 14.04 mT, which is the smallest magnetic field among maximum magnetic field values of the three coils (see Table I). However, the trajectory change from circle to ellipse and the radius of the trajectory become smaller with the increment of the rotating frequency, as the magnetic field generated by each coil has different amplitude and phase delay. These elliptical rotating magnetic fields generate torque ripple in (1) because the magnitude of the external magnetic field changes with time along the path of the ellipse. Once we assume that the magnetic moment of the helical robot is $1\ \mathrm{A \cdot m^2}$, the torque ripple can be calculated as shown in Fig. 3(d). In Fig. 3(d), the average magnetic torque decreases with an increase in the rotating frequency. However, the torque ripple has the greatest value at approximately 11 Hz, where the phase difference between the *x*- and *z*-directional magnetic fields has a relatively high value. The ripple and attenuation of the magnetic torque are undesirable because the helical robot needs large precise magnetic torques to clear obstructed regions.

C. Solution to the Inductance Effect: RLC Circuit

To overcome the inductance effect, we utilize the resonant effect of an *RLC* circuit. Since each coil of the conventional MNS has a resistance and an inductance, we include a variable capacitor to each coil of the proposed MNS. Then, the amplitude and the delayed phase of the output current of each coil can be expressed as follows [24]:

$$I_o = \frac{V_i}{\sqrt{{R_c}^2 + \left(2\pi f L_c - \frac{1}{2\pi f C_v}\right)^2}} \quad (8)$$

$$\phi = \tan^{-1}\left(\frac{2\pi f L_c}{R_c} - \frac{1}{2\pi f C_v R_c}\right) \quad (9)$$

where C_v is the capacitance of a variable capacitor. In (8) and (9), we can obtain the maximum current (V_i/R_c) and zero phase delay at the resonant frequency, expressed as follows:

$$f_r = \sqrt{\frac{1}{4\pi^2 C_v L_c}}. \quad (10)$$

Using (2), (8), (9), and Table I, the amplitudes and phase delays of the magnetic field generated by the proposed MNS with maximum input voltage can be calculated. Fig. 4(a) and (b) illustrates the calculated magnetic flux density and phase delay of each coil in which the proposed MNS has a resonant frequency of 50 Hz. While the conventional MNS decreases the magnetic field and induces a phase delay of 90° with an increase in the rotating frequency, the proposed MNS can generate maximal magnetic fields without phase delay at the resonant frequency. Fig. 4(c) shows the rotating magnetic field in the *xz*-plane according to the rotating frequency. Because we can adjust the resonant frequency by using variable capacitors, the rotating magnetic field always has a circular trajectory with a maximum magnetic field of 14.04 mT. Fig. 4(d) shows the torque ripple of the robot. Because the magnetic field magnitude does not change with time, we can obtain constant maximum magnetic torque without ripple, regardless of the rotating frequency.

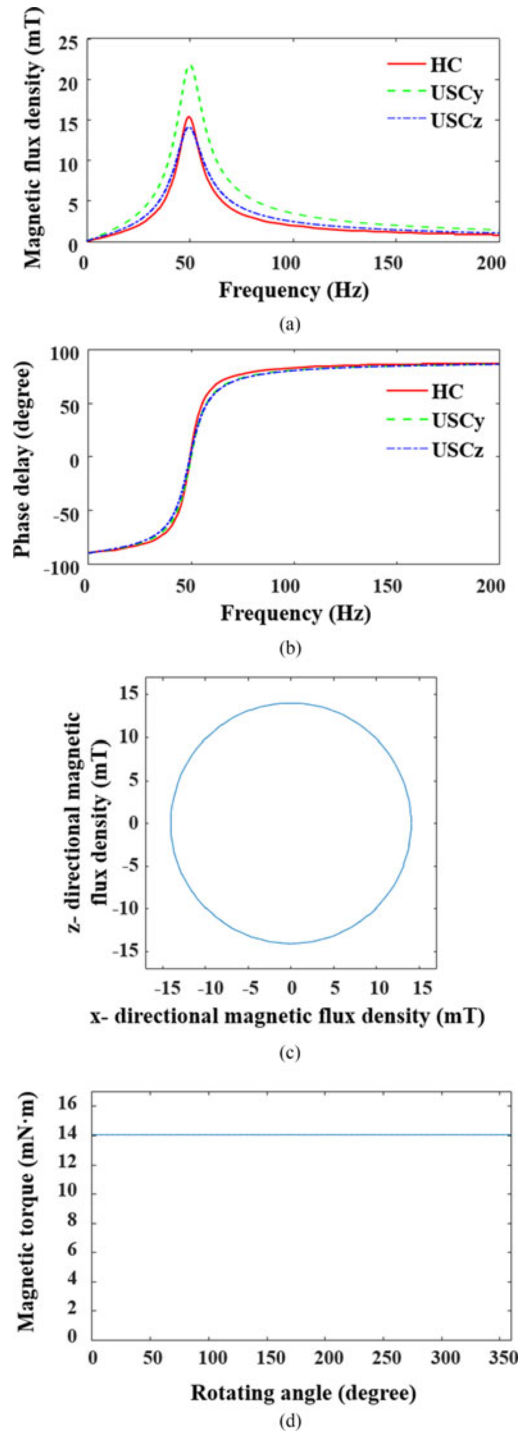

Fig. 4. (a) Magnetic flux density of each coil of the proposed MNS. (b) Phase delay of each coil of the proposed MNS. (c) Rotating magnetic field in the *xz*-plane with maximum amplitude regardless of frequency. (d) Constant magnetic torque in the *xz*-plane applied to the helical robot with a magnetic moment of $1\ \mathrm{A \cdot m^2}$.

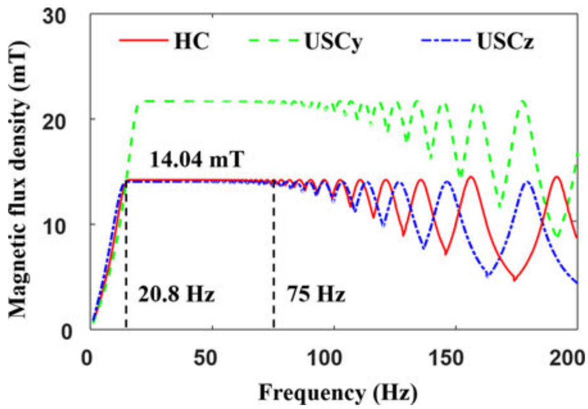

Fig. 5. Magnetic flux density of each coil of the proposed MNS.

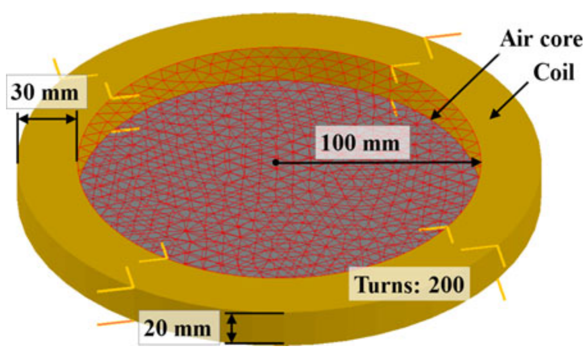

Fig. 6. Finite-element model with design parameters of the additional HC inductor.

III. Results and Discussion

A. Variable Capacitor and Additional Inductor

We constructed three variable capacitors able to change capacitance values from 1 to 299 μF by connecting two capacitors of 100 μF, nine capacitors of 10 μF, and nine capacitors of 1 μF in parallel with switches, as shown in Fig. 1. In (10), higher resonant frequencies necessitate smaller capacitance values, but the capacitor changes with a resolution of 1 μF such that we cannot generate every resonant frequency, especially at high frequencies. For this reason, the available magnetic flux density generated by each coil fluctuates at high frequencies, as shown in Fig. 5. Additionally, the maximum capacitance value is 299 μF, and the lowest HC, and USCz and USCy resonant frequencies of the proposed MNS are 14.7, 20.5, and 14.7 Hz, respectively.

We designed the additional inductor with the shape of a thin solenoid as shown in Fig. 6. We performed finite-element analysis and calculated the additional inductance to match the inductance of USCz with that of HC. We constructed the inductor and measured an inductance of 49.9 mH. The calculated inductance (47.7 mH) matched well with the measured value (49.9 mH). Fig. 7 shows the calculated magnetic flux density of each coil, where the resonant frequency is adjusted to the nearest input frequency using variable capacitors and an additional inductor. Using this additional inductor, the three orthogonal coils can generate the rotating magnetic field at the same resonant frequency, with maximum amplitude.

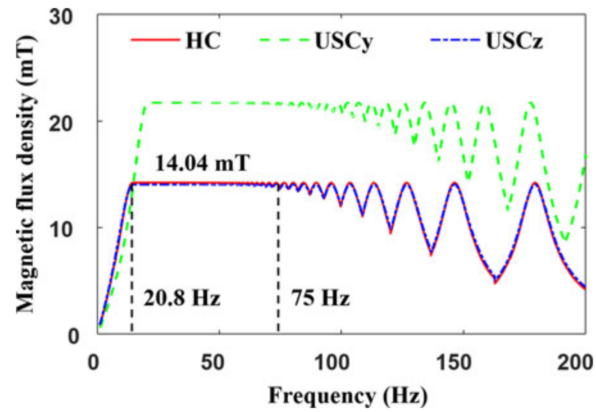

Fig. 7. Magnetic flux density of each coil of the proposed MNS with the additional inductor.

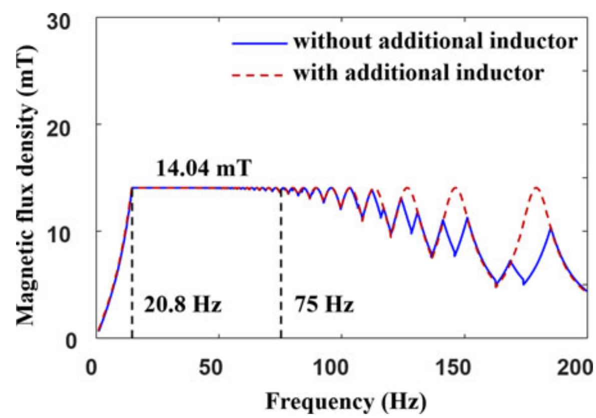

Fig. 8. Available maximum magnetic flux density in the proposed MNS with the effect of additional inductor to generate a rotating magnetic field.

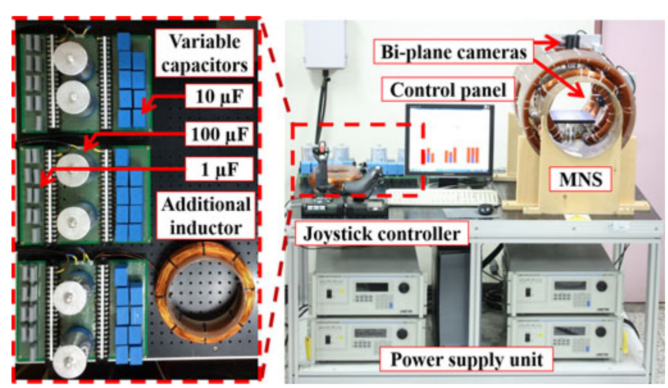

Fig. 9. Proposed MNS with variable capacitors and an additional inductor for the *RLC* circuit.

The available magnitude of a rotating magnetic field is determined by the minimum magnetic flux density among the maximum magnetic flux density of each coil, and it is the magnetic flux density of 14.04 mT generated by USCz. We generate a rotating magnetic field of 14.04 mT in the frequency range

TABLE II
CALCULATED AND MEASURED MAJOR VALUES IN HC, USC*y*, AND USC*z* OF THE PROPOSED MNS

	Resonant frequency (Hz)		Current amplitude (A)		Current phase delay (degree)		Magnetic flux density (mT)	
	Calculation	Measurement	Calculation	Measurement	Calculation	Measurement	Calculation	Measurement
HC	30.1	30.1	7.71	7.70	0	−0.3	14.18	14.17
	59.7	58.4	7.71	7.68	0	−0.7	14.18	14.12
	89.6	89.5	7.71	7.61	0	1.1	14.18	13.99
	126.7	126.0	7.71	7.63	0	−0.4	14.18	14.03
	179.2	178.4	7.71	7.60	0	0.9	14.18	13.97
USC*y*	30.1	30.4	7.63	7.60	0	0.4	21.69	21.60
	60.0	59.9	7.63	7.63	0	0.3	21.69	21.69
	91.6	91.6	7.63	7.56	0	−0.9	21.69	21.49
	125.4	125.9	7.63	7.51	0	1.1	21.69	21.35
	177.4	180.4	7.63	7.30	0	−1.2	21.69	20.75
USC*z*	30.1	30.1	7.78	7.78	0	0.2	14.04	14.04
	59.7	58.8	7.78	7.77	0	−0.5	14.04	14.02
	89.6	89.7	7.78	7.76	0	0.4	14.04	14.00
	126.7	126.4	7.78	7.77	0	0.8	14.04	14.02
	179.2	178.5	7.78	7.75	0	−0.7	14.04	13.98

between 20.5 and about 75 Hz without an additional inductor, as shown in Fig. 5. However, if we match the inductance value of each the coil as shown in Fig. 7, we can generate a rotating magnetic field of 14.04 mT at several frequencies over about 75 Hz. Thus, we add the additional inductor to USC*z* to match the inductance of USC*z* with that of HC. In the case of USC*y*, it generates large enough magnetic field than those of HC and USC*z*, as shown in Figs. 5 and 7, but the MNS uses only the amount of 14.04 mT from USC*y* to generate a rotating magnetic field which is determined by the minimum magnetic flux density among the maximum magnetic flux density of each coil. Therefore, USC*y* does not need the additional inductor. Fig. 8 shows available maximum magnetic flux density in the proposed MNS with the effect of additional inductor. Finally, the proposed MNS can generate a rotating magnetic field of 14.04 mT even over 75 Hz, as shown in Fig. 8.

B. Verification of the Constructed MNS

We constructed the MNS with *RLC* circuits as shown in Fig. 9. Robot locomotion was observed by biplane cameras and controlled via a joystick controller. To verify the proposed system, we measured the amplitude and phase delay of the current and magnetic flux density at several resonant frequencies. In the experiments, the magnetic field, current, and voltage of the MNS were measured with a Gauss probe, current probe, and voltage probe, respectively, and the phase delay of the current was determined by observing the output current with respect to input current. The Gauss probe is Model 6010 by F. W. Bell, and its measuring range is 0.1 μT to 30 T with the resolution of 0.1 μT. The current probe is AP015 by Le Croy, and its measuring range is 30 A with $\pm1\%$ accuracy. The voltage probe is ADP300 by Le Croy, and its measuring range is 400 V with $\pm1\%$ accuracy. The power supply is 3001iX by California Instruments, and it supplies 3 kW to the each coil with 0.5% accuracy.

Table II shows the calculated and measured values at several resonant frequencies, and the corresponding amplitudes and phase delays of the current and corresponding magnetic flux densities, respectively. As shown in Table II, errors between calculated and measured values increased with an increase in resonant frequency, as the distortions of an input voltage generated by the power supply unit increased with an increase in resonant frequency. However, the measured values corresponded well with the calculated values within an error margin of 5%.

C. Enhanced Helical Robot Locomotion

The step-out frequency is the maximum rotating frequency of a helical robot synchronized with an externally rotating magnetic field for the given magnetic moment and blade pitch of the robot, the external magnetic field, and the fluidic condition. It is one of the general indexes for evaluating the navigation and unclogging capabilities of helical robots [25]. To verify the enhanced capability of the robot in the proposed MNS, we measured the rotational frequency and step-out frequency of helical robots with different blade pitches, as shown in Fig. 10(a) and (b), and the rotational frequency of the robots was measured by CCLD Laser Tacho probe by B&K. Fig. 10(c) illustrates the swimming motion of robot A in a vertical watery tube. Fig. 11 shows the measured robot swimming speeds with increased rotating frequency in the conventional and proposed MNS. During the experiments, step-out frequencies were determined by measuring the frequency at which swimming speeds decreased drastically in a vertical tube, as the robots cannot synchronize with an external rotating magnetic field at that particular frequency. Table III shows the step-out frequencies of robots A and B in the conventional and proposed MNS. In the conventional MNS, robot B had a higher step-out frequency (46.3 Hz) than robot A (40.1 Hz), but the magnetic field applied to robot B at the step-out frequency (3.54 mT) was lower than that of robot A (4.05 mT) due to the inductance effect at high rotating frequencies. However, in the proposed MNS, both robots utilize the maximum rotating magnetic field (14.04 mT) at any rotating frequency, and the step-out frequency of robots

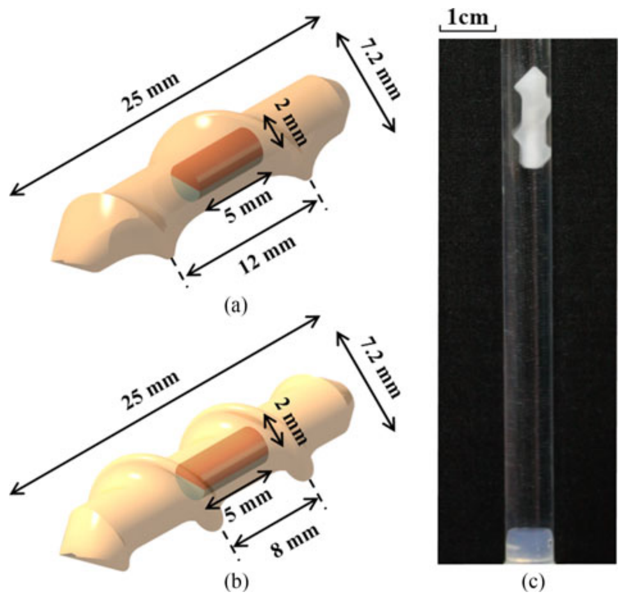

Fig. 10. (a) Helical robot A with a magnetic moment of 18.125 mA·m^2 and a blade pitch of 12 mm. (b) Robot B with a magnetic moment of 18.125 mA·m^2 and a blade pitch of 8 mm. (c) Swimming motion of robot A in a vertical tube (*f*: 30 Hz, B_0: 14.04 mT).

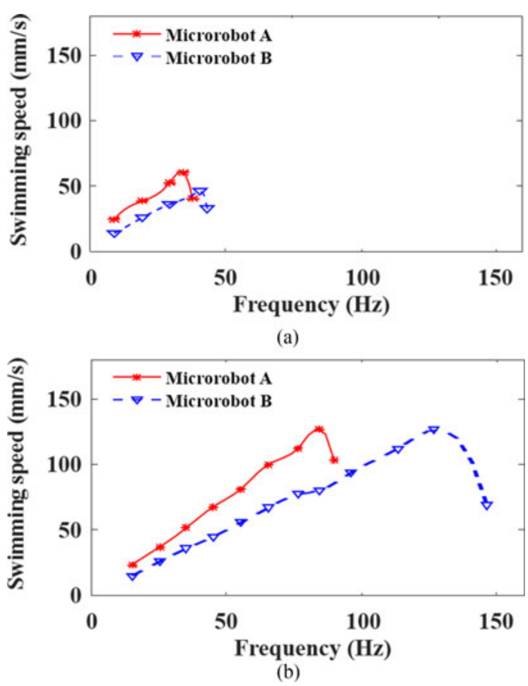

Fig. 11. (a) Swimming speeds of robots due to the rotating magnetic fields generated by the conventional MNS. (b) Swimming speeds of the robots due to the rotating magnetic fields generated by the proposed MNS.

A and B were 84.5 and 126.7 Hz, respectively. The increasing rate of a step-out frequency of robot B (274%) is greater than that of the robot A (211%) because the increasing rate of the applied magnetic field to robot B (297%) is greater than that of the robot A (247%).

TABLE III
STEP-OUT FREQUENCY OF THE HELICAL MICROROBOTS

	Step-out frequency (Hz)	
	Conventional MNS	Proposed MNS
Robot A	40.1	84.5
Robot B	46.3	126.7

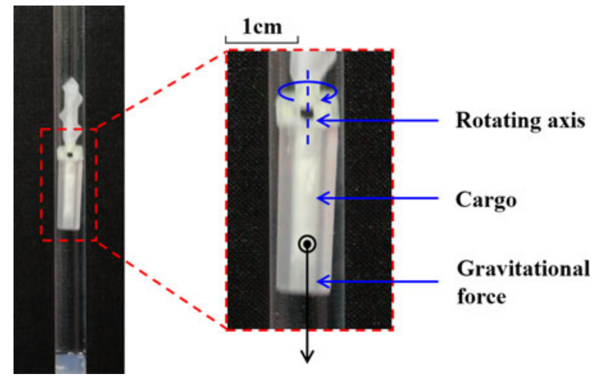

Fig. 12. Cargo delivery motion of robot A in a vertical tube (*f*: 50 Hz, B_0: 14.04 mT).

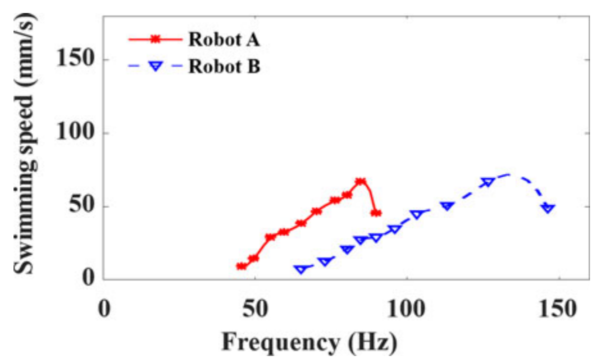

Fig. 13. Swimming speeds of robots with cargo due to the rotating magnetic fields generated by the proposed MNS.

Since the proposed MNS substantially improves the step-out frequency and swimming speeds of robots, we also investigated robot cargo-carrying capacity. Fig. 12 shows the cargo-carrying motion of robot A in the proposed MNS, with a cargo load of 1 g (robot weight = 0.5 g). Fig. 13 shows measured swimming speeds of robots with cargo in the proposed MNS. Overall, robot speeds decreased, as the gravitational force of the cargo decreases the thrust force generated by the magnetic torque. However, the step-out frequencies were unchanged, because the step-out frequency is only dependent upon the magnetic moment and blade pitch of the robot, the external magnetic field, and the fluidic condition. Using the improved carrying capacity of the proposed MNS, the robots may perform various tasks, such as drug delivery in human blood vessels.

Fig. 14 outlines the drilling experiments used to compare the unclogging capability of helical robot B in the conventional and

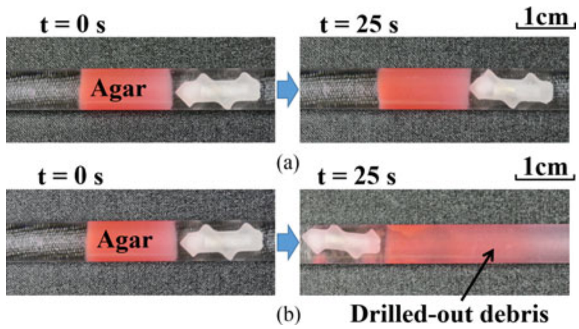

Fig. 14. Comparison of the unclogging motion of robot B in a clogged tube (diameter = 10 mm) utilizing rotating magnetic fields with step-out frequencies generated by (a) the conventional MNS (*f*: 46.3 Hz, B_0: 3.54 mT) and (b) the proposed MNS (*f*: 126.7 Hz, B_0: 14.04 mT).

proposed MNS. To simulate an obstructed blood vessel, agar (diameter = 10 mm, length = 25 mm) was situated in a tube. During the experiment, the rotational frequencies of both MNS were set to be the step-out frequencies in Table III which make the robot B drill with the fastest speed. The robot B in the conventional MNS, which generates a rotating magnetic field of 3.54 mT at 46.3 Hz, could not penetrate the obstructed area. However, the robot B in the proposed MNS, which generates a rotating magnetic field of 14.04 mT at 126.7 Hz, completed the unclogging mission in 25 s, while the robot B cannot even rotate at the same frequency in conventional MNS (*f*: 126.7 Hz, B_0: 1.32 mT), as shown in Fig. 11(a).

IV. Conclusion

In this paper, we proposed an effective method to generate improved moving and unclogging motion of helical robots utilizing a novel MNS with the resonant effect of an *RLC* circuit. The coil inductance effect of the proposed MNS was effectively reduced at the resonant frequency of the *RLC* circuit, and the resonant frequency was regulated using variable capacitors and an additional inductor. The constructed MNS was verified by measuring several resonant frequencies, the amplitude and phase of the current, and the magnetic fields at certain resonant frequencies. Using the proposed MNS, we experimentally observed improved movement and unclogging capabilities of a helical robot in 2-D environments. There are still several design, control, and safety issues of the helical robot with the application of the proposed MNS. One of them is to manipulate the helical robot in complicated 3-D blood vessels with advanced robot control methodology. However, this research can contribute to applying the magnetic robots to perform various medical tasks in human blood vessels to replace the conventional operations using wired catheters.

References

[1] J. Park, D. Hyun, W. Cho, T. Kim, and H. Yang, "Normal-force control for an in-pipe robot according to the inclination of pipelines," *IEEE Trans. Ind. Electron.*, vol. 58, no. 12, pp. 5304–5310, Dec. 2011.

[2] H. Huang, J. Yan, and T. Cheng, "Development and fuzzy control of a pipe inspection robot," *IEEE Trans. Ind. Electron.*, vol. 57, no. 3, pp. 1088–1095, Mar. 2010.

[3] B. Kim, S. Lee, J. H. Park, and J.-O. Park, "Design and fabrication of a locomotive mechanism for capsule-type endoscopes using shape memory alloys (SMAs)," *IEEE/ASME Trans. Mechatronics*, vol. 10, no. 1, pp. 77–86, Feb. 2005.

[4] S. Guo, T. Fukuda, and K. Asaka, "A new type of fish-like underwater microrobot," *IEEE/ASME Trans. Mechatronics*, vol. 8, no. 1, pp. 136–141, Mar. 2003.

[5] Y. Guozheng, L. Qiuhong, D. Guoqing, and Y. Detian, "The prototype of a piezoelectric medical microrobot," in *Proc. 2002 Int. Symp. Micromechatron. Hum. Sci.*, 2002, pp. 73–77.

[6] P. Dario, M. C. Carrozza, C. Stefanini, and S. D'Attanasio, "A mobile microrobot actuated by a new electromagnetic wobble micromotor," *IEEE/ASME Trans. Mechatronics*, vol. 3, no. 1, pp. 9–16, Mar. 1998.

[7] L. Chen, S. Liu, Y. C. Zhou, and T. J. Cui, "An optimizable circuit structure for high-efficiency wireless power transfer," *IEEE Trans. Ind. Electron.*, vol. 60, no. 1, pp. 339–349, Jan. 2013.

[8] L. Yan, T. Wang, D. Liu, J. Peng, Z. Jiao, and C.-Y. Chen, "Capsule robot for obesity treatment with wireless powering and communication," *IEEE Trans. Ind. Electron.*, vol. 62, no. 2, pp. 1125–1133, Feb. 2015.

[9] B. J. Nelson, I. K. Kaliakatsos, and J. J. Abbott, "Microrobots for minimally invasive medicine," *Annu. Rev. Biomed. Eng.*, vol. 12, no. 1, pp. 55–85, 2010.

[10] S. H. Kim and K. Ishiyama, "Magnetic robot and manipulation for active-locomotion with targeted drug release," *IEEE/ASME Trans. Mechatronics*, vol. 19, no. 5, pp. 1651–1659, Oct. 2014.

[11] S. Yim, K. Goyal, and M. Sitti, "Magnetically actuated soft capsule with the multimodal drug release function," *IEEE/ASME Trans. Mechatronics*, vol. 18, no. 4, pp. 1413–1418, Aug. 2013.

[12] D. Lloyd-Jones *et al.*, "Heart disease and stroke statistics—2009 update a report from the American heart association statistics committee and stroke statistics subcommittee," *Circulation*, vol. 119, no. 3, pp. 480–486, Jan. 2009.

[13] L. Wen, T. Wang, G. Wu, J. Liang, and C. Wang, "Novel method for the modeling and control investigation of efficient swimming for robotic fish," *IEEE Trans. Ind. Electron.*, vol. 59, no. 8, pp. 3176–3188, Aug. 2012.

[14] X. Niu, J. Xu, Q. Ren, and Q. Wang, "Locomotion learning for an anguilliform robotic fish using central pattern generator approach," *IEEE Trans. Ind. Electron.*, vol. 61, no. 9, pp. 4780–4787, Sep. 2014.

[15] K. E. Peyer, S. Tottori, F. Qiu, L. Zhang, and B. J. Nelson, "Magnetic helical micromachines," *Chem., Eur. J.*, vol. 19, no. 1, pp. 28–38, Jan. 2013.

[16] S. M. Jeon, G. H. Jang, and W. S. Lee, "Drug-enhanced unclogging motions of a double helical magnetic micromachine for occlusive vascular diseases," *IEEE Trans. Magn.*, vol. 50, no. 11, pp. 1–4, Nov. 2014.

[17] S. Jeong, H. Choi, K. Cha, J. Li, J. Park, and S. Park, "Enhanced locomotive and drilling microrobot using precessional and gradient magnetic field," *Sens. Actuators Phys.*, vol. 171, no. 2, pp. 429–435, Nov. 2011.

[18] S. H. Kim, K. S. Shin, S. Hashi, and K. Ishiyama, "A pushing force mechanism of magnetic spiral-type machine for wireless medical-robots in therapy and diagnosis," *IEEE Trans. Magn.*, vol. 49, no. 7, pp. 3488–3491, Jul. 2013.

[19] M. P. Kummer, J. J. Abbott, B. E. Kratochvil, R. Borer, A. Sengul, and B. J. Nelson, "OctoMag: An electromagnetic system for 5-DOF wireless micromanipulation," in *Proc. IEEE Int. Conf. Robot. Autom.*, 2010, pp. 1610–1616.

[20] H. Choi, K. Cha, S. Jeong, J.-O. Park, and S. Park, "3-D locomotive and drilling microrobot using novel stationary EMA system," *IEEE/ASME Trans. Mechatronics*, vol. 18, no. 3, pp. 1221–1225, Jun. 2013.

[21] S. Jeon, G. Jang, H. Choi, and S. Park, "Magnetic navigation system with gradient and uniform saddle coils for the wireless manipulation of micro-robots in human blood vessels," *IEEE Trans. Magn.*, vol. 46, no. 6, pp. 1943–1946, Jun. 2010.

[22] S. M. Jeon, G. H. Jang, J. H. Choi, S. H. Park, and J. O. Park, "Precise manipulation of a microrobot in the pulsatile flow of human blood vessels using magnetic navigation system," *J. Appl. Phys.*, vol. 109, no. 7, p. 07B316, Apr. 2011.

[23] S. M. Jeon, G. H. Jang, H. C. Choi, S. H. Park, and J. O. Park, "Magnetic navigation system for the precise helical and translational motions of a microrobot in human blood vessels," *J. Appl. Phys.*, vol. 111, no. 7, p. 07E702, Apr. 2012.

[24] D. Halliday, R. Resnick, and J. Walker, *Fundamentals of Physics Extended*. New York, NY, USA: Wiley, 2010.

[25] K. Ishiyama, M. Sendoh, and K. I. Arai, "Magnetic micromachines for medical applications," *J. Magn. Magn. Mater.*, vols. 242–245, Part 1, pp. 41–46, Apr. 2002.

Jaekwang Nam received the B.S. degree in mechanical engineering from Hanyang University, Seoul, South Korea, in 2011, where he is currently working toward the Ph.D. degree in mechanical convergence.

His research interests include various structures of microrobots performing multifunction in human blood vessels and their magnetic navigation systems.

Wonseo Lee (S'16) received the B.S. degree in mechanical engineering from Hanyang University, Seoul, South Korea, in 2014, where he is currently working toward the Ph.D. degree in mechanical convergence engineering.

His current research interests include design, analysis, and control of magnetic robots and magnetic catheters with electromagnetic systems for biomedical applications.

Bongjun Jang received the B.S. degree in mechanical engineering from Gachon University, Gyeonggi-do, South Korea, in 2015. He is currently working toward the M.S. degree in mechanical convergence engineering at Hanyang University, Seoul, South Korea.

His current research interests include design, analysis, and control of magnetic robots and electromagnetic systems for biomedical applications.

Gunhee Jang (M'00) received the B.S. degree from Hanyang University, Seoul, South Korea in 1984, the M.S. degree from Korea Advanced Institute of Science and Technology, Seoul, in 1986, and the Ph.D. degree from the University of California, Berkeley, CA, USA, in 1993, all in mechanical engineering.

He is currently a Professor in the Department of Mechanical Engineering and the Director of the Precision Rotating Electromechanical Machine Laboratory, Hanyang University. He has authored or coauthored more than 280 articles published in journals and conference proceedings in his field and more than 29 patents including several international patents. His current research is focused on microrobots actuated by magnetic navigation systems, and electromechanical systems, such as motors and actuators.